ChemComm

COMMUNICATION

View Article Online
View Journal | View Issue

Cite this: *Chem. Commun.*, 2023, 59, 3122

Received 1st February 2023,
Accepted 15th February 2023

DOI: 10.1039/d3cc00468f

rsc.li/chemcomm

Crystal structure engineering of metal halide perovskites for photocatalytic organic synthesis†

Chunhua Wang,[a] Yang Ding,[b] Biao Liu,[c] Bo Weng,*[d] Johan Hofkens*[ae] and Maarten B. J. Roeffaers*[d]

Engineering crystal structure of Cs_3BiBr_6 and $Cs_3Bi_2Br_9$ is theoretically and experimentally demonstrated to modulate their photocatalytic performance. This work offers insights into the structure-photoactivity relationships of metal halide perovskites (MHPs) and provides a guideline for exploiting MHPs toward efficient photocatalytic organic synthesis.

Semiconductor-based photocatalysis has attracted growing attention in solar-to-chemical energy conversion.[1] The basic principle of photocatalysis starts at the electronic band structure of the semiconductors, which dominates the optoelectronic properties and drives the charge carrier that underpin their photocatalytic properties.[2] Consequently, the semiconductor crystal structure, which determines the electronic band structures, as well as the photogenerated charge carrier dynamics, is a key factor affecting their photocatalytic performance.[3] For example, anatase TiO_2 has often been reported to exhibit better photoactivity than the rutile crystal phase, originating from the difference in photogenerated charge generation and transfer.[4,5] Similarly, tetragonal $BiVO_4$ was reported to be less active as a photocatalyst than monoclinic scheelite $BiVO_4$.[6] In short, the photocatalytic performance of semiconductors can be regulated *via* crystal structure engineering.

Inspired by the great advances in solar cells,[7,8] metal halide perovskites (MHPs) have recently emerged as promising photocatalysts due to their excellent optoelectronic properties.[9–11] Among them, lead-free Bi-based compounds such as $Cs_3Bi_2Br_9$ show excellent stability.[12] However, most MHP materials generally exhibit modest photocatalytic performance due to ineffective charge separation and sluggish surface reaction. To improve photoactivity, cocatalyst loading[9,13] and heterojunction construction[10,11] are effective. On the other hand, the crystalline structure of MHPs has been shown to play a key role in modulating photoactivity.[13] For instance, the incorporation of heteroatoms Ag[13] and Sb[14] into $Cs_3Bi_2Br_9$ leads to form $Cs_2AgBiBr_6$ and $Cs_3SbBiBr_9$, which could improve the photoactivity as compared with $Cs_3Bi_2Br_9$. However, $Cs_2AgBiBr_6$ and $Cs_3SbBiBr_9$ are intrinsic different from $Cs_3Bi_2Br_9$, making it difficult to directly uncover the relationship between crystal structures and photocatalytic performance of MHPs. Therefore, it is anticipated to explore the exact effect of crystal structure on photoactivity based on the MHPs with same elements while different crystalline structures.

Herein, the effect of crystal structure in Cs_3BiBr_6 and $Cs_3Bi_2Br_9$ on the photocatalytic performance is investigated. Density functional theory (DFT) calculations reveal that the photogenerated charge carriers in $Cs_3Bi_2Br_9$ have a reduced effective mass, lower exciton binding energy, and longer carrier lifetime than that in Cs_3BiBr_6. Photoelectrochemical characterizations further confirm that $Cs_3Bi_2Br_9$ exhibits improved charge transfer efficiency as compared with Cs_3BiBr_6. When applied to photocatalytic benzyl alcohol (BA) oxidation, $Cs_3Bi_2Br_9$ displays enhanced photocatalytic performance compared to Cs_3BiBr_6. Further decoration of these MHPs with Pd nanocubes as cocatalysts, the BA conversion over 1 wt% Pd/$Cs_3Bi_2Br_9$ (82.3%) is over twice than that of 1 wt% Pd/Cs_3BiBr_6 (39.5%). This work offers mechanistic insights into the structure-photoactivity of MHPs and provides a guideline for rational design of efficient MHP photocatalysts.

DFT calculations were first performed to understand the crystal structures of $Cs_3Bi_2Br_9$ and Cs_3BiBr_6. For $Cs_3Bi_2Br_9$, within the unit cell (Fig. 1A, Table S1, ESI†), eight Cs^+ ions occupied the corners and two other Cs^+ ions located on the body diagonal of the unit cell,[13] and Bi atoms occupy partial Br_6

[a] *Department of Chemistry, KU Leuven, Celestijnenlaan 200F, Leuven 3001, Belgium. E-mail: johan.hofkens@kuleuven.be*
[b] *Laboratory of Inorganic Materials Chemistry (CMI), University of Namur, 61 rue de Bruxelles, B-5000, Namur, Belgium*
[c] *Hunan Key Laboratory for Super-microstructure and Ultrafast Process, School of Physics and Electronics, Central South University, Changsha 410083, P. R. China*
[d] *cMACS, Department of Microbial and Molecular Systems, KU Leuven, Celestijnenlaan 200F, Leuven 3001, Belgium. E-mail: maarten.roeffaers@kuleuven.be, bo.weng@kuleuven.be*
[e] *Max Planck Institute for Polymer Research, Ackermannweg 10, Mainz 55128, Germany*

† Electronic supplementary information (ESI) available. See DOI: https://doi.org/10.1039/d3cc00468f

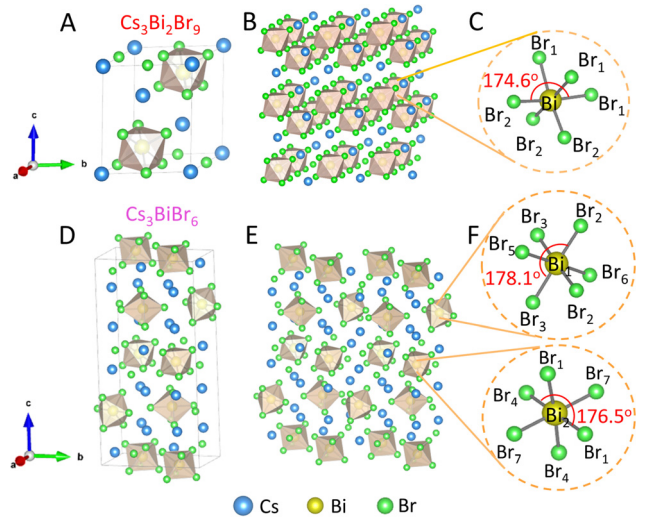

Fig. 1 (A) The unit cell of $Cs_3Bi_2Br_9$. (B) Three-dimensional structure of $Cs_3Bi_2Br_9$ material. (C) Bi–Br bonds and the angles of Br_1–Bi–Br_2 of $BiBr_6$ octahedra in $Cs_3Bi_2Br_9$. (D) The unit cell of Cs_3BiBr_6 material. (E) Three-dimensional structure of Cs_3BiBr_6. (F) Bi–Br bonds and the typical Br_2–Bi_1–Br_3 and Br_7–Bi_2–Br_7 angles of $BiBr_6$ octahedra in Cs_3BiBr_6.

holes in an ordered arrangement (Fig. 1B), where three short and three long Bi–Br bonds with shorter linkages are shared between neighboring octahedra in each layer (Fig. 1C, Table S2, ESI†).[13] The local coordination environment of the $[BiBr_6]^{3-}$ octahedra is irregular and leads to a trigonal distortion, forming a two-dimensional perovskite structure. Cs_3BiBr_6, by contrast, contains two Bi atoms, three Cs atoms, and seven Br atoms in an asymmetric unit (Fig. 1D). These two Bi atoms are independent (Fig. 1F), where each Bi atom is coordinated by six Br atoms and the bond lengths of Bi–Br are different (Table S2, ESI†), and the bond angle between Br–Bi–Br in Cs_3BiBr_6 is distorted.[15] The $[BiBr_6]^{3-}$ octahedra exist in isolation and no link between these octahedra, forming a zero-dimensional perovskite structure (Fig. 1E).[15,16] Then, the band structures and density of states (DOS) of both materials were studied. From the energy band structures (Fig. S1, ESI†), the conduction band minimum (CBM) and valence band maximum (VBM) of $Cs_3Bi_2Br_9$ are more dispersive than those of Cs_3BiBr_6, hinting that the $Cs_3Bi_2Br_9$ has lower effective masses of electrons and holes (*vide infra*).[13] For $Cs_3Bi_2Br_9$, the VBM primarily consists of Br 4p states and Bi 6p orbitals, mixed with a few Bi 6s states (Fig. S1B, ESI†), and the CBM is dominated by Bi 6p and Br 4p orbital interactions.[17] For Cs_3BiBr_6, the VBM is mainly composed of Br 4p orbitals, and the CBM consists of an admixture of Bi 6p and Br 4p orbitals (Fig. S1D, ESI†).

The photoelectric properties of $Cs_3Bi_2Br_9$ and Cs_3BiBr_6 can be assessed by physical factors such as exciton binding energy, effective mass, charge mobility, and charge carrier relaxation time.[13] These parameters were calculated and listed in Table 1. The exciton binding energy (E_b) of $Cs_3Bi_2Br_9$ is calculated to be 0.278 eV, much smaller than that of Cs_3BiBr_6 (0.505 eV), which is beneficial for the separation of photogenerated excitons and extraction of charge carriers.[13] Besides, $Cs_3Bi_2Br_9$ shows a

Table 1 Calculated electron and hole effective masses (m^*), carrier mobility (μ), corresponding relaxation time (τ), exciton binding energy (E_b), and bandgap (E_g) for $Cs_3Bi_2Br_9$ and Cs_3BiBr_6

Parameter	$Cs_3Bi_2Br_9$	Cs_3BiBr_6
m_e^* (m_e)	0.57	1.42
m_h^* (m_h)	5.46	6.32
μ_e (m^2 V^{-1} S^{-1})	4.89×10^{-1}	6.34×10^{-2}
τ_e (fs)	1585.3	512.03
E_b (eV)	0.278	0.505
E_g (eV)	2.596	3.195

significant drop in effective mass of charge carriers as compared to Cs_3BiBr_6; calculated electron effective mass 0.57 m_e ($Cs_3Bi_2Br_9$) *vs.* 1.42 m_e (Cs_3BiBr_6) and the effective hole mass reduces from 6.32 m_h to 5.46 m_h. Generally, the smaller the effective mass of charge carriers, the faster the transfer rate of charges.[10] Thus, the lower effective mass in $Cs_3Bi_2Br_9$ links to higher mobility which is beneficial for charge carriers migration.[13] This is confirmed by the calculated carrier mobility, where the value of $Cs_3Bi_2Br_9$ is higher than that of Cs_3BiBr_6. Also, their different deformation potential constants (Fig. S2, ESI†) agree with the results of effective mass and carrier mobility. Furthermore, $Cs_3Bi_2Br_9$ possesses a longer carrier relaxation time than Cs_3BiBr_6, which responds to the prolonged carrier lifetime in $Cs_3Bi_2Br_9$.

Next, $Cs_3Bi_2Br_9$ and Cs_3BiBr_6 were synthesized (see ESI†) for further analysis.[18] XRD results in Fig. 2A show that both $Cs_3Bi_2Br_9$ and Cs_3BiBr_6 exhibit strong diffraction peaks, without shift compared to theoretical data. $Cs_3Bi_2Br_9$ has a trigonal crystalline structure,[19] while Cs_3BiBr_6 crystallizes in an orthorhombic phase.[15] Raman spectroscopy (Fig. 2B) reveals the modes at 167 and 192 cm^{-1} in $Cs_3Bi_2Br_9$ belonging to the stretching vibrations of Bi–Br bonds in the $[BiBr_6]^{3-}$ octahedra.[20] For Cs_3BiBr_6, although

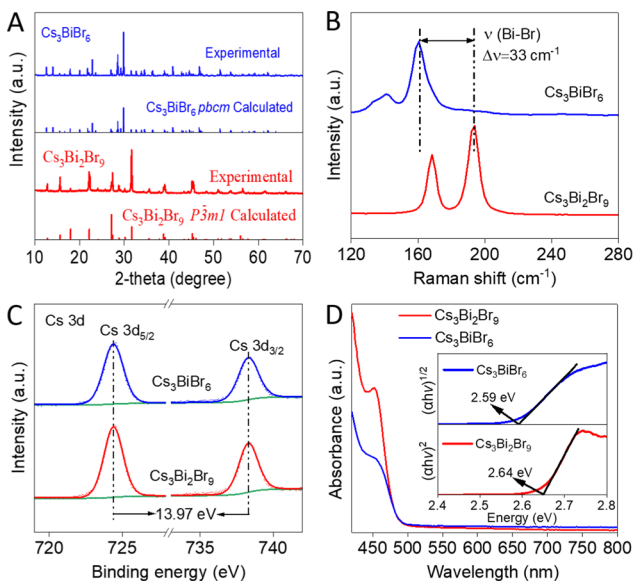

Fig. 2 (A) XRD patterns, (B) Raman spectra, (C) high-resolution XPS spectra of Cs 3d core levels, and (D) DRS spectra of $Cs_3Bi_2Br_9$ and Cs_3BiBr_6 materials. The inset in Fig. 2D shows the bandgaps of both materials.

it also contains $[BiBr_6]^{3-}$ octahedra, the complex groups are isolated and do not share corners, yielding peaks at different frequencies, *i.e.* 160 and 135 cm^{-1}. By contrast, Cs_3BiBr_6 showed a red-shift (33 cm^{-1}) for the terminal Bi–Br stretching modes of the $[BiBr_6]^{3-}$ octahedra compared to $Cs_3Bi_2Br_9$, which suggests weaker Bi–Br bonds in Cs_3BiBr_6,[16] in line with the slightly longer Bi–Br bond lengths (Table S2, ESI†).

XPS was performed to investigate the chemical structure and valence state of both materials. The signals of Cs 3d (Fig. 2C), Bi 4f and Br 3d (Fig. S3A and B, ESI†) are the same, confirming their expected valence states (+1, +3, and −1, respectively) to be consistent with the formula.[15,16] The stoichiometry in $Cs_3Bi_2Br_9$ was calculated to be Cs : Bi : Br = 3 : 2.21 : 9.20, and for Cs_3BiBr_6 the ratio is Cs : Bi : Br = 3 : 1.22 : 6.37 (Table S3, ESI†), close to their theoretical values. SEM images (Fig. S4, ESI†) show that both materials have a similar particle size of about 500 nm. EDX spectroscopy further confirms the presence of Cs, Bi and Br elements (Fig. S4E and F, ESI†). Nitrogen physisorption data (Fig. S5, ESI†) shows that the surface area of both materials is similar (Table S4, ESI†).

UV-Vis DRS was employed to determine their absorption properties (Fig. 2D). Note that although $Cs_3Bi_2Br_9$ and Cs_3BiBr_6 have different elemental compositions and structures, they have in common $[BiBr_6]^{3-}$ octahedra, and their optical properties are largely determined by the Bi^{3+} cation levels, perturbed slightly by the environment surrounding $[BiBr_6]^{3-}$octahedra.[20,21] The absorption onset of $Cs_3Bi_2Br_9$ is measured at 470 nm (2.64 eV),[18] and for Cs_3BiBr_6 it is 479 nm (2.59 eV),[15] which is consistent with their colors (Fig. S6, ESI†). The extracted bandgap of $Cs_3Bi_2Br_9$ agrees with DFT calculation as well as reported results,[18] while Cs_3BiBr_6 shows a difference (0.6 eV) with the calculated one which could be attributed to the DFT limitations.[15] Mott–Schottky analyses (Fig. S7, ESI†), combined with UV-Vis data, show that CB and VB edge potentials of $Cs_3Bi_2Br_9$ and Cs_3BiBr_6 are −0.57 and 2.07 eV, and −0.69 and 1.9 eV (*vs.* NHE), respectively. Steady-state PL spectrum (Fig. S8, ESI†) shows that $Cs_3Bi_2Br_9$ has an emission centered at around 469 nm, which almost coincides with its bandgap (2.64 eV), corresponding to near band edge emission.[13] The emission peak of Cs_3BiBr_6 shows a slight blue shift, which could be attributed to its indirect bandgap property.[22]

Photoelectrochemical measurements were further performed to reveal the picture of charge separation and transfer.[23] Fig. 3A shows the transient photocurrent responses of both materials, where a higher photocurrent is observed for $Cs_3Bi_2Br_9$ than that of Cs_3BiBr_6, suggesting the efficient charge separation in $Cs_3Bi_2Br_9$.[24] To better understand the difference, EIS experiments were performed.[23] Clearly, $Cs_3Bi_2Br_9$ presents a smaller semicircle in the Nyquist plots (Fig. S9, ESI†), confirming the efficient transfer of charge carriers in $Cs_3Bi_2Br_9$.[24–26] This is further corroborated by the surface charge transfer efficiency (η_t) measurements[25,27] (Fig. 3B), the η_t of $Cs_3Bi_2Br_9$ and $Cs_3Bi_2Br_9$ is calculated to be 24% and 31%, respectively. To conclude, the above observations disclose that $Cs_3Bi_2Br_9$ would empower faster charge carriers injection into the redox couple during the photocatalytic reaction.[10,24]

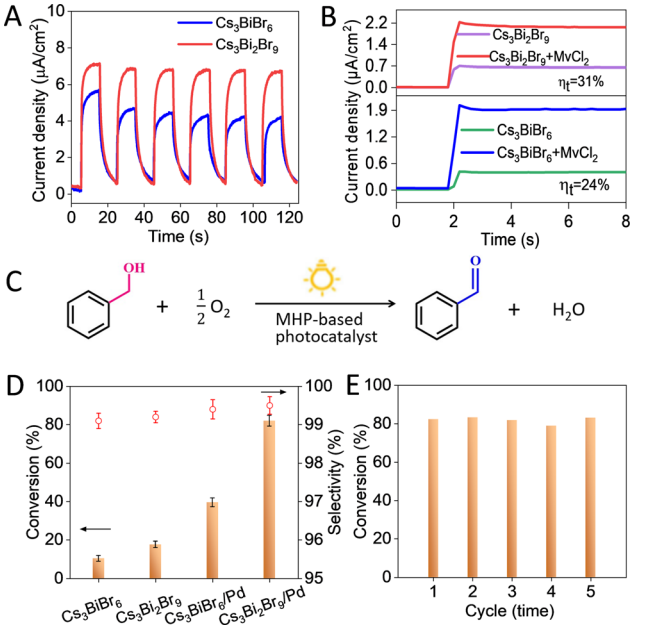

Fig. 3 (A) Transient photocurrent, (B) surface charge transfer efficiency (η_t) of $Cs_3Bi_2Br_9$ and Cs_3BiBr_6. (C) Schematic illustration of photocatalytic selective oxidation of benzyl alcohol (BA) to benzaldehyde (BAD) under simulated solar light illumination. (D) The photocatalytic performance of selective BA oxidation over various photocatalysts. (E) Stability test of Pd/$Cs_3Bi_2Br_9$ composite. Reaction conditions: 0.1 mmol BA in 2.5 mL molecular oxygen saturated benzotrifluoride, 15 mg catalyst, simulated solar light (AM 1.5G, 150 W Xe lamp), reaction time (6 h).

The selective photocatalytic oxidation of benzyl alcohol (BA) was used as model reaction to compare the performance of $Cs_3Bi_2Br_9$ and Cs_3BiBr_6 (Fig. 3C, see Scheme S1, ESI†); the band edge energies of both materials are suitable for the involved redox potentials (+ 0.68 eV).[28] $Cs_3Bi_2Br_9$ shows a higher BA conversion (17.5%) than Cs_3BiBr_6 (10.2%) after solar light irradiation of 6 h (Fig. 3D), with an excellent selectivity (over 99%) towards benzaldehyde (BAD). To further enhance photoactivity, Pd nanocubes were deposited on MHPs surfaces. The 1 wt% Pd/$Cs_3Bi_2Br_9$ composite converts 82.3% BA, over 2-fold enhancement than 1 wt% Pd/Cs_3BiBr_6 (39.5%). This is attributed to the fact that Pd serves as an electron reservoir to promote the transfer of photogenerated charge carriers, thus improving the conversion of BA.[27] Besides, a comparison of $Cs_3Bi_2Br_9$/Pd with reported photocatalysts for selective BA oxidation shows the excellent performance of this material (Table S5, ESI†). Moreover, recycling tests show that no activity loss for 1 wt% Pd/$Cs_3Bi_2Br_9$ is observed after 5 successive cycles (Fig. 3E). Additionally, the catalyst is stable after exposing in air for 15 days (Fig. S10, ESI†), and no crystal structure changes are observed in XRD patterns (Fig. S11, ESI†).

To elucidate the reation mechanism over Pd/$Cs_3Bi_2Br_9$ sample, control experiments using different radical scavengers were performed (Fig. S12, ESI†). When hole scavenger ammonium oxalate was added, the conversion rate shows a sharp drop, indicating the key role of photogenerated holes in driving this reaction.[10] Contrarily, the performance remains with electron

(potassium persulfate) or $^{\bullet}O_2^-$ (1,4-benzoquinone) scavengers.[10,29] This follows that O_2 was trapped by electrons to produce $^{\bullet}O_2^-$ radicals, while the generated $^{\bullet}O_2^-$ is not directly involved in the BA oxidation process.[23] Moreover, when the O_2 is replaced by argon (Ar), an obvious reduction in the activity was observed, showing that O_2 reacted with electrons which can effectively promote the separation of charge carriers so that this reaction can proceed smoothly. In addition, the presence of hydroxyl radicals ($^{\bullet}OH^-$) scavenger, *t*-butanol, has a negligible effect on the performance since no $^{\bullet}OH^-$ existed in this reaction system.[23] Based on these experiments, we propose a plausible mechanism (Fig. S13, Scheme S1, ESI†). Under light illumination, $Cs_3Bi_2Br_9$ absorbs solar light to produce electron-hole pairs. The photogenerated electrons migrate to the surface of Pd and reduce O_2 to $^{\bullet}O_2^-$, and the generated holes activate BA and generate the BAD product.[23]

In summary, the effect of the crystal structure of Cs_3BiBr_6 and $Cs_3Bi_2Br_9$ on optoelectronic properties and ultimately photocatalytic performance, was investigated theoretically and experimentally. DFT results showed that $Cs_3Bi_2Br_9$ has a smaller carrier effective mass, lower exciton binding energy, and higher charge mobility than Cs_3BiBr_6. Furthermore, the more efficiency in charge separation within the $Cs_3Bi_2Br_9$ than Cs_3BiBr_6 was experimentally confirmed. As a result, $Cs_3Bi_2Br_9$ material exhibited a boosted photocatalytic BA oxidation performance, over twice higher than Cs_3BiBr_6. This work systematically illustrates the crystal structure-photoactivity relationship of MHPs and offers a guideline for exploiting excellent MHP photocatalysts.

This work was financially supported by the Research Foundation - Flanders (FWO grants G098319N, 1280021N), the KU Leuven Research Fund (C14/19/079, iBOF-21-085 PERSIST), KU Leuven Industrial Research Fund (C3/19/046), the Flemish government through long term structural funding Methusalem (CASAS2, Meth/15/04), and MPI financial support to J.H. as an MPI fellow. C.W. acknowledges the financial support from the China Scholarship Council (201806370198). Open Access funding provided by the Max Planck Society.

Conflicts of interest

There are no conflicts to declare.

References

1 Y. Ding, S. Maitra, S. Halder, C. Wang, R. Zheng, T. Barakat, S. Roy, L.-H. Chen and B.-L. Su, *Matter*, 2022, **5**, 2119–2167.
2 Y. He, Y. Liu, C. Li, X.-B. Chen, Z. Shi and S. Feng, *ACS Appl. Energy Mater.*, 2022, **5**, 8923–8929.
3 Y. Ding, S. Maitra, C. Wang, S. Halder, R. Zheng, T. Barakat, S. Roy, L. H. Chen and B. L. Su, *Interdiscip. Mater.*, 2022, **1**, 213–255.
4 T. Luttrell, S. Halpegamage, J. Tao, A. Kramer, E. Sutter and M. Batzill, *Sci. Rep.*, 2014, **4**, 1–8.
5 J. Zhang, P. Zhou, J. Liu and J. Yu, *Phys. Chem. Chem. Phys.*, 2014, **16**, 20382–20386.
6 G. L. Chiarello, A. D. Paola, L. Palmisano and E. Selli, *Photochem. Photobiol. Sci.*, 2011, **10**, 355–360.
7 C. Wang, C. Zhang, S. Wang, G. Liu, H. Xia, S. Tong, J. He, D. Niu, C. Zhou, K. Ding, Y. Gao and J. Yang, *Sol. RRL*, 2018, **2**, 1700209.
8 M. A. Green, A. Ho-Baillie and H. J. Snaith, *Nat. Photonics*, 2014, **8**, 506–514.
9 M. Roy, S. Ghorui, Bhawna, J. Kangsabanik, R. Yadav, A. Alam and M. Aslam, *J. Phys. Chem. C*, 2020, **124**, 19484–19491.
10 C. Wang, H. Huang, B. Weng, D. Verhaeghe, M. Keshavarz, H. Jin, B. Liu, H. Xie, Y. Ding and Y. Gao, *Appl. Catal., B*, 2022, **301**, 120760.
11 H. Huang, D. Verhaeghe, B. Weng, B. Ghosh, H. Zhang, J. Hofkens, J. A. Steele and M. B. Roeffaers, *Angew. Chem.*, 2022, e202203261.
12 W. Xiang, S. Liu and W. Tress, *Energy Environ. Sci.*, 2021, **14**, 2090–2113.
13 M. Shi, G. Li, W. Tian, S. Jin, X. Tao, Y. Jiang, E. A. Pidko, R. Li and C. Li, *Adv. Mater.*, 2020, **32**, e2002137.
14 M. Shi, H. Zhou, W. Tian, B. Yang, S. Yang, K. Han, R. Li and C. Li, *Cell Rep. Phys. Sci.*, 2021, **2**, 100656.
15 Y. Tang, M. Liang, B. Chang, H. Sun, K. Zheng, T. Pullerits and Q. Chi, *J. Mater. Chem. C*, 2019, **7**, 3369–3374.
16 H. Yang, T. Cai, E. Liu, K. Hills-Kimball, J. Gao and O. Chen, *Nano Res.*, 2020, **13**, 282–291.
17 T. Geng, S. Wei, W. Zhao, Z. Ma, R. Fu, G. Xiao and B. Zou, *Inorg. Chem. Front.*, 2021, **8**, 1410–1415.
18 C. Wang, B. Weng, Y. Liao, B. Liu, M. Keshavarz, Y. Ding, H. Huang, D. Verhaeghe, J. A. Steele and W. Feng, *Chem. Commun.*, 2022, **58**, 10691–10694.
19 B. Yang, J. Chen, F. Hong, X. Mao, K. Zheng, S. Yang, Y. Li, T. Pullerits, W. Deng and K. Han, *Angew. Chem., Int. Ed.*, 2017, **56**, 12471–12475.
20 M. N. Tran, I. J. Cleveland and E. S. Aydil, *J. Mater. Chem. C*, 2020, **8**, 10456–10463.
21 S. E. Creutz, H. Liu, M. E. Kaiser, X. Li and D. R. Gamelin, *Chem. Mater.*, 2019, **31**, 4685–4697.
22 J. Eichhorn, S. P. Lechner, C.-M. Jiang, G. F. Heunecke, F. Munnik and I. D. Sharp, *J. Mater. Chem. A*, 2021, **9**, 20653–20663.
23 H. Huang, C. Zhou, X. Jiao, H. Yuan, J. Zhao, C. He, J. Hofkens, M. B. Roeffaers, J. Long and J. A. Steele, *ACS Catal.*, 2019, **10**, 1439–1443.
24 B. Weng, Q. Quan and Y.-J. Xu, *J. Mater. Chem. A*, 2016, **4**, 18366–18377.
25 Y. Ding, S. Maitra, C. Wang, R. Zheng, M. Zhang, T. Barakat, S. Roy, J. Liu, Y. Li and T. Hasan, *J. Energy Chem.*, 2022, **70**, 236–247.
26 T. Chen, B. Weng, S. Lu, H. Zhu, Z. Chen, L. Shen, M. B. Roeffaers and M.-Q. Yang, *J. Phys. Chem. Lett.*, 2022, **13**, 6559–6565.
27 C. Wang, B. Weng, M. Keshavarz, M.-Q. Yang, H. Huang, Y. Ding, F. Lai, I. Aslam, H. Jin and G. Romolini, *ACS Appl. Mater. Interfaces*, 2022, **14**, 17185–17194.
28 Y. Wu, X. Ye, S. Zhang, S. Meng, X. Fu, X. Wang, X. Zhang and S. Chen, *J. Catal.*, 2018, **359**, 151–160.
29 H. Huang, H. Yuan, J. Zhao, G. Solís-Fernández, C. Zhou, J. W. Seo, J. Hendrix, E. Debroye, J. A. Steele, J. Hofkens, J. Long and M. B. J. Roeffaers, *ACS Energy Lett.*, 2018, **4**, 203–208.